Polímeros
ISSN 1678-5169 (Online)
(cc) BY
https://doi.org/10.1590/0104-1428.20260025

ORIGINAL ARTICLE

# Injection overmolded polyamide 6 - Eucalyptus joints

**Giovana Zanetini Zanchetta[1], Gean Henrique Marcatto de Oliveira[2], Matheus Furlan[1], Vinicius Fiocco Sciuti[1], Rodrigo Bresciani Canto[1], Sergio de Traglia Amancio-Filho[2] and Leonardo Bresciani Canto[1]***

*[1]Programa de Pós-graduação em Ciência e Engenharia de Materiais – PPGCEM, Universidade Federal de São Carlos – UFSCar, São Carlos, SP, Brasil*

*[2]Institute of Materials Science, Joining and Forming – Professorship "Aviation Materials and Manufacturing Techniques", Graz University of Technology, Graz, Austria*

**leonardo@ufscar.br*

## Abstract

The development of polymer–wood joints addresses the growing demand for lightweight and environmentally sustainable structures. This study reports the development of joints combining polyamide 6 and *Eucalyptus grandis*, produced via direct-adhesion injection overmolding. Scanning electron microscopy (SEM) and X-ray microtomography analyses revealed a well-defined interface, with PA6 penetrating open wood vessels and forming protrusions (~50 µm) that promote mechanical interlocking. Mechanical testing showed good repeatability, with the joints reaching shear strength values up to 8.1 ± 0.6 MPa, which are comparable to those reported in the literature for polymer–wood overlap joints. Digital image correlation (DIC), coupled with mechanical tests, further indicated a more uniform strain distribution along the interface for the single-chamfer geometry, suggesting more efficient stress transfer during mechanical overloading.

**Keywords:** *direct-adhesion, hybrid joint, injection overmolding, wood.*

**Data Availability:** All data supporting the findings of this study are included in this article.

**How to cite:** Zanchetta, G. Z., Oliveira, G. H. M., Furlan, M., Sciuti, V. F., Canto, R. B., Amancio-Filho, S. T., & Canto, L. B. (2026). Injection overmolded polyamide 6 - Eucalyptus joints. *Polímeros: Ciência e Tecnologia*, *36*(3), e20260034. https://doi.org/10.1590/0104-1428.20260025

## 1. Introduction

Hybrid structures combining polymers with other materials enable the synergistic integration of their most advantageous properties, fostering the design of advanced structural components. For instance, polymer–metal joints can combine the low density, chemical resistance, and shape flexibility of polymers with the high stiffness and strength of metals[1].

Meanwhile, the growing demand for sustainable materials has intensified research into renewable alternatives aimed at reducing environmental impact. Among renewable materials, natural wood has attracted interest due to its high strength-to-weight ratio, comparable to those of steel and aluminum alloys, in addition to its thermal and electrical insulation, good machinability, favorable acoustic properties, aesthetic appeal, abundance, and low cost. Furthermore, in addition to its ability to sequester $CO_2$, wood production requires relatively low energy input and results in lower environmental impacts than polymers and metals[2-4].

Proper integration of wood with polymers in hybrid structures offers a promising strategy to combine the low density, renewability, and favorable mechanical performance of wood with the durability, processability, and design flexibility of polymers, thereby reducing environmental impact while maintaining functional performance. Such hybrid structures are particularly attractive for automotive applications[5], including interior components and selected structural elements, where lightweight and sustainability are key requirements.

Injection overmolding stands out as an efficient and industrially viable technique for producing polymer-based structures, as it enables polymer shaping and joining to the substrate in a single, fast, precise, and automated step[6-8]. This process allows precise control of parameters known to affect interfacial adhesion, such as polymer viscosity, pressure, and contact time[6,7]. Moreover, the organic chemical composition and naturally porous morphology of wood favor direct adhesion with polymers, eliminating the need for adhesives or additional interlayers. Since the wood substrate is exposed to relatively low temperatures and short residence times during injection overmolding, thermal degradation is avoided, allowing joining with engineering and specialty polymers beyond polyolefins.

A recent study demonstrated the feasibility of producing mechanically robust polymer–wood joints by direct-adhesion injection overmolding. Stadlmann et al.[9] evaluated the lap-shear strength of polypropylene (PP)- and polyamide 6 (PA6)-based joints with birch (*Betula pendula Roth.*) and beech (*Fagus sylvatica* L.) hardwoods. Using SEM, the authors demonstrated that interfacial adhesion is governed by polymer penetration into surface wood vessels and fibers,

with penetration depths of approximately 100-200 µm. PA6 joints exhibited significantly higher shear strength than PP joints (approximately 6 MPa versus 2 MPa), with no statistically significant differences observed between the two wood species. This behavior was attributed to the higher polarity of PA6, which promotes stronger interfacial interactions and more effective bonding with the wood surface.

Among the various wood species available for hybrid structures, *Eucalyptus grandis* is particularly attractive due to its wide availability from fast-growing plantations. This species presents a favorable combination of relatively high mechanical strength and low density, which is desirable for lightweight applications. In addition, its porous anatomical structure, characterized by the presence of vessels and fibers with relatively large lumens[10], may facilitate polymer penetration and mechanical interlocking during injection overmolding.

In this study, joints composed of polyamide 6 and *Eucalyptus grandis* wood were developed by direct-adhesion injection overmolding. Two novel scarf-joint geometries with single- and double-chamfer configurations were designed and evaluated. The deformation behavior was investigated by mechanical testing coupled with digital image correlation (DIC), while the joining mechanisms were analyzed using scanning electron microscopy (SEM) and X-ray microtomography.

## 2. Materials and Methods

### 2.1 Materials

Polyamide 6 (PA6) is a medium-viscosity grade (Ultramid® C 200) supplied by BASF, with a density of 1.14 g $cm^{-3}$ (ISO 1183), and is designed for injection molding. The PA6 pellets were dried in a vacuum oven at 60 °C for 12 h. This material was chosen because it is an engineering thermoplastic widely used as a matrix in polymer composites for structural and engineering applications.

*Eucalyptus grandis* wood was obtained in the form of 1-inch-thick boards, which were dried at room temperature until reaching moisture equilibrium. The boards were then cut using a circular saw into bars with dimensions of 91 × 12.8 × 3.2 $mm^3$ (length × width × thickness), taking into account the anisotropy and morphology of the wood and maintaining the longitudinal fiber orientation. Subsequently, chamfers were machined at one end of the bars using a circular saw in single (straight) and double (V-shaped) configurations, both with 45° angles.

### 2.2 Injection overmolding

PA6−Eucalyptus joints with single- and double-chamfer scarf configurations (Figure 1) were employed. The geometry and dimensions of the joint specimens were adapted from ASTM D638 Type I tensile specimens, enabling the use of standard injection-molding cavities commonly available in research and development laboratories. The 45° scarf chamfers impose a combination of tensile and shear stresses at the interface when the joints are subjected to uniaxial tensile loading.

The joints were produced using a Battenfeld Plus 35/75 injection molding machine. The machine was operated in semi-automatic mode, where the wood piece was manually placed in the mold cavity before initiating the injection molding cycle. The injection molding parameters were set as follows: barrel temperature profile of 220/230/240 °C, injection speed of 21 $cm^3$ $s^{-1}$, holding pressure of 160 bar, holding time of 9 s, mold temperature of 30 °C, and cooling time of 40 s.

### 2.3 Mechanical testing

The mechanical tests were carried out following a procedure adapted from ASTM D638, using an Instron 5569 universal testing machine. The distance between grips was set to 115 mm, and the tests were performed at a crosshead speed of 1 mm $min^{-1}$. The specimens were conditioned in a desiccator for 48 h prior to the tests, which were conducted at 23 °C and 50% relative humidity. Five specimens were tested to determine the values of ultimate force and displacement.

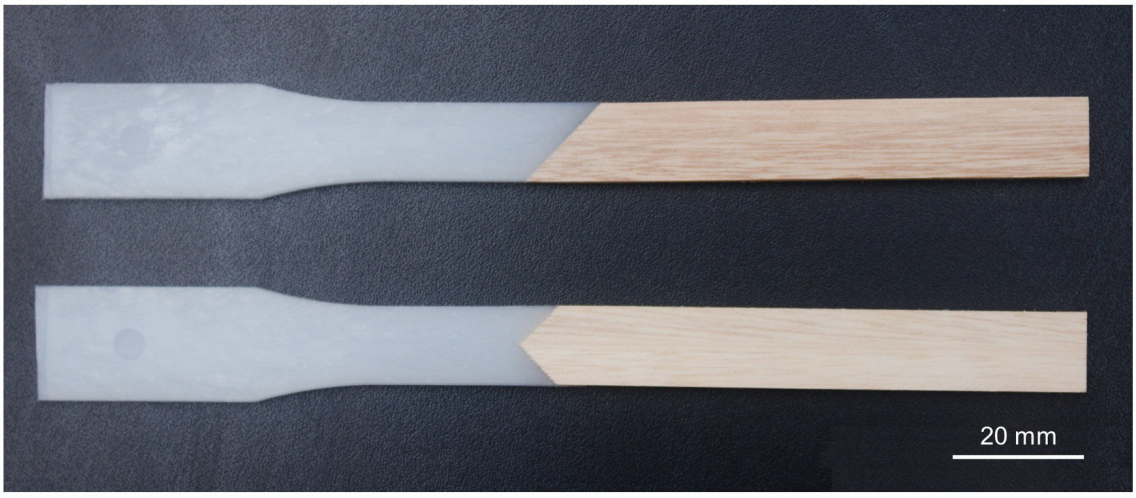



**Figure 1.** Photographs of PA6–Eucalyptus scarf joints with single- and double- chamfer configurations. The geometry and dimensions of the joint specimens were adapted from ASTM D638 Type I tensile specimens. The thickness of the specimens is 3.2 mm.

### 2.4 Scanning electron microscopy

The mid-thickness of the joints were examined by scanning electron microscopy (SEM) using an FEI Inspect S50 microscope operated at an accelerating voltage of 5 kV and equipped with a secondary electron (SE) detector. The joints were sectioned at a distance of approximately 5 mm from the interface, cold-mounted in epoxy resin with a curing time of 24 h, and sequentially ground using P120, P240, P600, and P1200 grit sandpapers until reaching half of the specimen thickness, followed by polishing with a synthetic felt cloth. Finally, the samples were gold-coated, electrically grounded using silver paint, and analyzed.

The fracture surfaces of the joints after mechanical testing were also analyzed by SEM using the same FEI Inspect S50 instrument operated at an accelerating voltage of 5 kV. The specimens were mounted on aluminum stubs and subsequently gold-coated and electrically grounded with silver paint prior to examination.

### 2.5 Microtomography

Micro-computed tomography (μCT) imaging was performed using a Werth TomoScope XS 160 system. The sample was sectioned approximately 5 mm from the interface and secured onto polystyrene foam supports. Acquisition parameters included a tube voltage of 80 kV, a current of 360 μA, and an exposure time of 1/3 s. A rotation step angle of 0.15° was used with a voxel size of 8.7 μm. Additionally, a 0.5 mm copper filter was employed to reduce beam hardening artifacts. Dragonfly software was utilized to process 2-D images obtained from μCT scans, generating 3-D volumetric reconstructions.

### 2.6 Mechanical testing with digital image correlation

Digital image correlation (DIC) was coupled with the mechanical tests to compute the strain fields of the PA6−Eucalyptus joints. The mechanical tests were performed using an MTS Exceed E44.304 universal testing machine equipped with a 30 kN maximum capacity load cell, screw-tightened clamping grips, and universal joints. The tests were carried-out at a crosshead speed of 1 mm $min^{-1}$. All mechanical tests were conducted in a climate-controlled room at a temperature of 23 ± 2 °C and a relative humidity of 50 ± 5%. The DIC hardware parameters are summarized in Table 1. Two cameras were positioned on opposite sides to simultaneously capture the front and back surfaces of the joint. Four cold white LED lamps were positioned diagonally at each side to ensure homogeneous illumination.

**Table 1.** DIC hardware parameters.

| Camera | Canon EOS 5DS |
|---|---|
| Lens | Canon EF 180 mm f/3.5L Macro USM |
| Gray level amplitude | 14 bits |
| Color filter | Bayer |
| Aperture | f/7.1 |
| Stand-off distance | 750 mm |
| Shutter speed | 1/30s |
| ISO | 100 |
| Resolution | 2920 × 4363 px |

The joints were spray-coated with white paint and subsequently speckled with black spray paint to generate a random speckle pattern, enabling full-field displacement tracking throughout the test. For image acquisition, after applying a 10 N preload, 20 initial images were recorded to define the reference configuration, i.e., to evaluate the measurement uncertainty associated with the experimental setup, followed by the acquisition of one image every 2 s during the mechanical test. The speckle images were analyzed using Correli 3.0 software[11] to compute the full-field displacement and strain maps developed during the mechanical test. A mesh composed of linear triangular finite elements (T3) was adopted, with an average characteristic element size of 100 px (≈ 3 mm). Virtual strain gauges with dimensions of 10 × 10 $mm^2$ were defined on each joint component, corresponding to a region containing approximately 25 elements (highlighted in green in Figure 2).

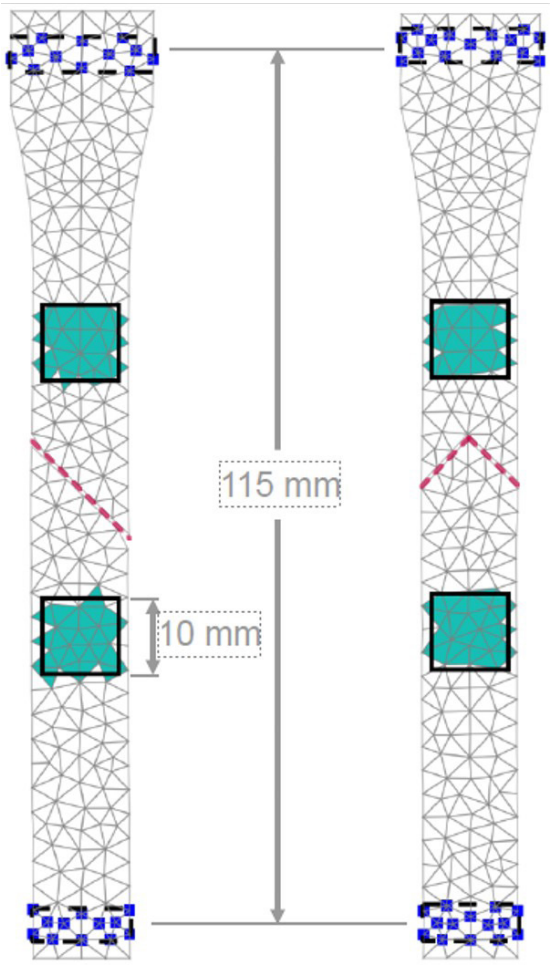



**Figure 2.** Schematic illustration of the specimens with single (left) and double (right) chamfer configurations and the digital image correlation (DIC) setup used for data analysis, showing the triangular finite-element mesh (T3) with an average characteristic element size of 100 px (≈ 3 mm), the positioning of virtual strain gauges (10 × 10 $mm^2$) on each joint component, and the virtual longitudinal extensometer with a gauge length of 115 mm used to monitor the overall joint displacement.

Within these regions, the strain components obtained from the DIC analysis were extracted, namely the longitudinal strain ($\varepsilon_y$), transverse strain ($\varepsilon_x$), and shear strain ($\varepsilon_{xy}$). The strain values reported for each virtual gauge correspond to the average of these components over the elements contained in the selected region, which reduces local measurement noise and provides a more robust estimate of the strain state. In addition, a virtual longitudinal extensometer with a gauge length of 115 mm (highlighted in blue in Figure 2) was defined to monitor the overall deformation of the joint. The elongation of the specimen was calculated from the difference in the longitudinal displacement component of the nodes located at the extremities of the gauge length. This procedure allows the global longitudinal strain of the specimen to be obtained directly from the displacement field.

Beyond the measurements obtained from the virtual strain gauges and the virtual extensometer, the strain field over the entire joint was also analyzed. Spatial maps of an equivalent scalar strain measure ($\varepsilon_{eq}$) were evaluated to characterize the deformation distribution within the specimen, particularly along the joint interface. The equivalent strain was computed from the in-plane strain components obtained from the DIC analysis. As a simplified assumption, a plane-strain state ($\varepsilon_z = \varepsilon_{xz} = \varepsilon_{yz} = 0$) was adopted, resulting in Equation 1[12,13]:

$$\varepsilon_{eq} = \frac{2}{3} \cdot \sqrt{\varepsilon_x^2 + \varepsilon_y^2 - \varepsilon_x \varepsilon_y + 3\varepsilon_{xy}^2} \quad (1)$$

This scalar quantity provides a convenient measure of the local strain intensity and is used in the following sections to visualize the spatial distribution of strain concentration in the joint specimens.

## 3. Results and Discussion

### 3.1 Polymer-wood interface

The mid-thickness SEM images of PA6−Eucalyptus scarf joints with single- and double-chamfer configurations are shown in Figure 3. The presented micrographs are representative of the features observed along the entire joint interface. For both joint configurations, well-defined interfaces are observed (Figure 3a and 3c), suggesting good wetting of the wood surface by molten PA6 during the injection overmolding process. Similar behavior was reported by Stadlmann et al.[9] for PA6–hardwood lap joints produced by injection overmolding, attributed to the low viscosity and polar nature of PA6, which promote effective wetting of wood constituents containing hydroxyl groups. SEM analysis further reveals penetration of PA6 into the wood substrate, indicated by the green arrows in Figure 3, images b and d. This feature is randomly distributed along the joint interface and exhibits characteristic dimensions on the order of 50 µm. The good wettability of PA6 on the eucalyptus cross-section promotes polymer spreading and penetration into the open lumens and surface irregularities of the wood during injection molding, favoring mechanical

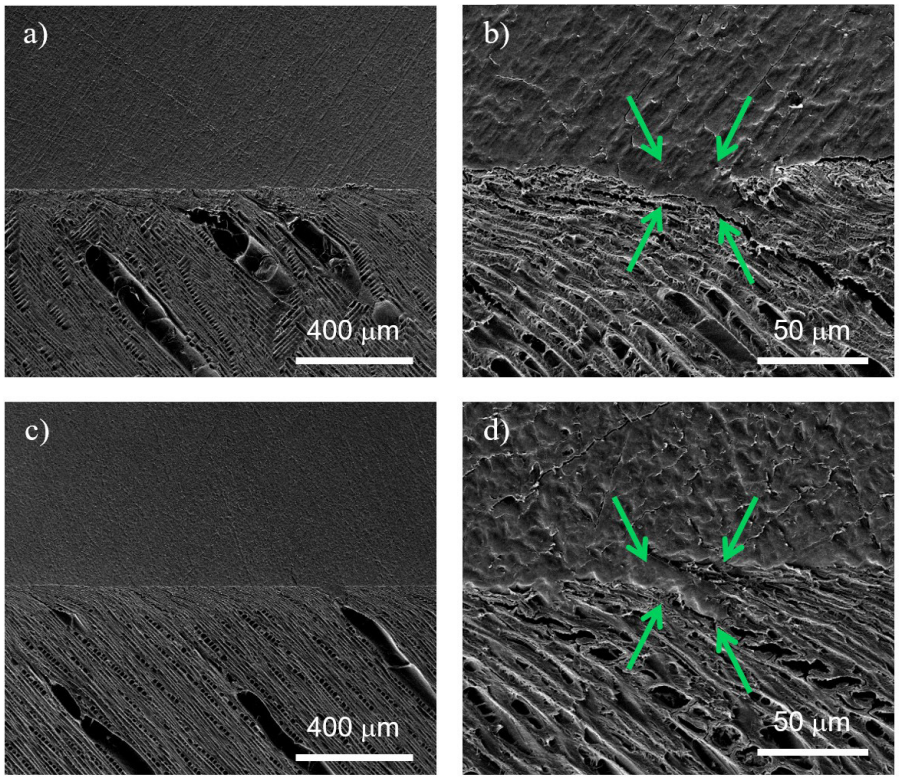



**Figure 3.** Mid thickness SEM images of PA6–Eucalyptus scarf joints with single- (a,b) and double- (c,d) chamfer configurations. The polymer is located at the top and the wood at the bottom. The sample was rotated 45° to position the polymer-wood interface in the horizontal direction.

interlocking and interfacial interactions, such as hydrogen bonding, due to the hydrophilic nature of both components[14]. The porous and anisotropic cellular structure of the wood is also evident, with vessels predominantly oriented along the fiber direction and diameters ranging from 10 to 50 µm.

SEM observations of the chamfered wood surface prior to joining (Figure 4) indicate that the circular saw machining partially collapsed vessels near the surface. This feature is also visible in the SEM images of the transverse cross-sections of the joints, extending over a layer of approximately 100 µm below the interface (Figure 3, images a and c). Nevertheless, some open vessels remain exposed, with diameters comparable to the polymer protrusions observed in the joints (Figure 3, images b and d), suggesting that these features act as mechanical sites for polymer penetration during injection overmolding.

The X-ray microtomography image in Figure 5 reveals the penetration of the polymer into an open wood vessel, indicated by the green arrows. The image also allows the identification of the interface between the polymer and the wood, as well as the collapse of wood vessels in a layer located below the interface, as previously discussed. The analysis indicates a polymer penetration depth of approximately 50 µm, a value consistent with that observed in the SEM images presented in Figures 3 and 4.

### 3.2 Polymer-wood mechanical behavior

The statistical distribution of the ultimate force and displacement for the PA6–Eucalyptus scarf joints with single- and double-chamfer configurations is presented in the box plots shown in Figure 6. For both joint configurations, the box plots exhibit narrow interquartile ranges and short whiskers, with mean and median values in close agreement, indicating low data dispersion, limited skewness, and high repeatability among the tested specimens. This aspect is particularly relevant for the hybrid system investigated, as local variations in wettability, polymer penetration into wood vessels, and differential shrinkage can significantly influence mechanical performance.

The joint shear strength was approximately estimated assuming a uniform shear stress distribution on the 45° chamfer plane, given by $\tau_{45^o} = F / 2A$, where $F$ is the ultimate force recorded during testing and $A$ is the nominal cross-sectional area of the specimen. Accordingly, the average shear strength of the PA6–Eucalyptus scarf joints was 8.1 ± 0.6 MPa and 7.3 ± 1.0 MPa for the single- and double-chamfer configurations, respectively, values comparable to those reported in the literature for overlap polymer–wood joints, such as PA6–birch (5.7 ± 1.1 MPa) and PA6–beech (6.4 ± 1.5 MPa) produced by injection overmolding[9], PA6-15CF–beech (7.5 ± 1.2 MPa) manufactured by fused filament fabrication[15], and PA6-15CF–oak (9.2 ± 0.7 MPa) joined by ultrasonic joining[16]. It should be noted that, unlike overlap joints which experience significant load eccentricity and secondary bending[17], the interface of the scarf polymer−wood joints investigated here are predominantly subjected to in-plane shear with superimposed normal stresses due to the chamfered interface.

### 3.3 Fractography

Figure 7 shows photographs of PA6–Eucalyptus scarf joints with single- (a) and double- (b) chamfer configurations after mechanical testing.

The single-chamfer joints exhibited two distinct macroscopic failure modes. Three specimens showed mixed failure characterized by partial delamination and fracture on the PA6 side, whereas the remaining two specimens failed by interfacial delamination. In contrast, all five specimens of the double-chamfer configuration exhibited mixed failure, also characterized by partial delamination and fracture on the PA6 side.

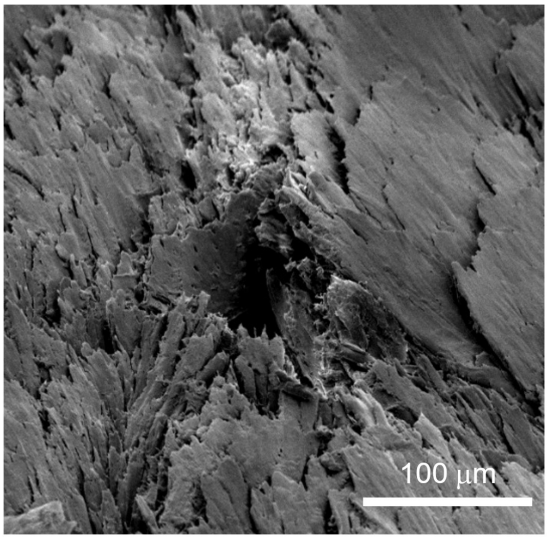



**Figure 4.** SEM images of the chamfered surface of the wood substrate prior to joining with polymer.

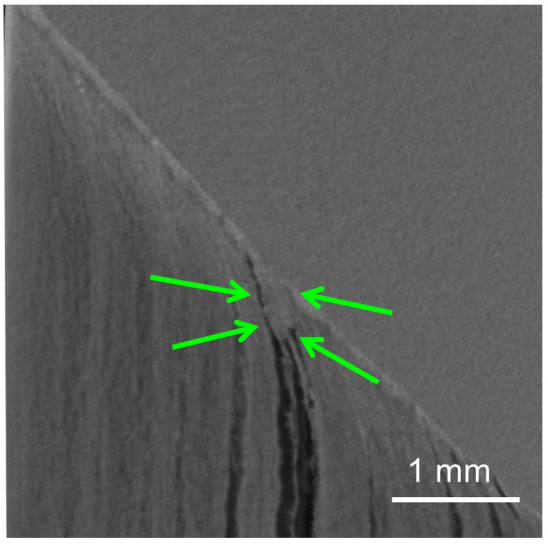



**Figure 5.** Microtomography image showing the filling of a wood vessel by the polymer. The polymer is located in the upper portion of the image, and the wood in the lower portion. The 45° chamfer angle was maintained, and the figure was not rotated.

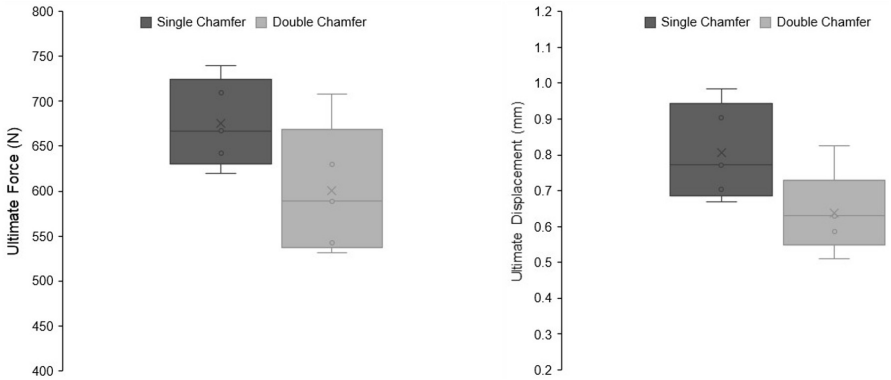



**Figure 6.** Box plots of the ultimate force and displacement values obtained from the mechanical tests of PA6–Eucalyptus scarf joints in single- and double-chamfer configuration.

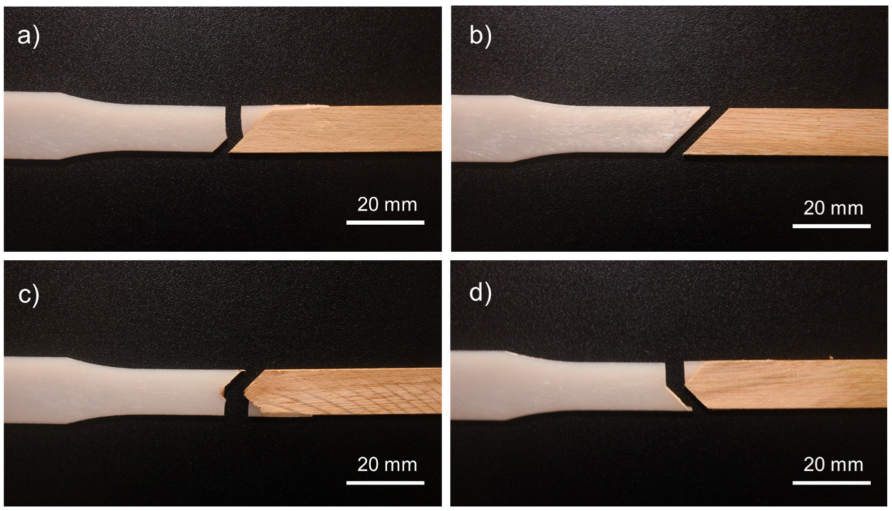



**Figure 7.** Photographs of PA6–Eucalyptus scarf joints with single- (a,b) and double- (c,d) chamfer configurations after mechanical testing.

Figure 8 shows representative SEM images of the delaminated fracture surfaces of PA6–Eucalyptus scarf joints. Protrusions (~50 µm) on the PA6 surface and corresponding cavities on the wood surface (labeled 1–6) indicate mechanical interlocking at the interface, while wood fragments adhered to the PA6 surface indicate localized cohesive failure within the wood substrate. Overall, these features indicate a mixed adhesive–cohesive fracture mode.

### *3.4 Digital image correlation*

Figure 9 presents the stress–strain curves obtained from mechanical tests coupled with DIC for the PA6–Eucalyptus scarf joints in the single- and double-chamfer configurations, with results shown separately for the joint as a whole, for the PA6 component, and for the wood component, corresponding to the two faces of the joint.

The global response of the joint (measured by the virtual longitudinal extensometer) lies between the individual responses of the components (measured by the virtual strain gauges), exhibiting intermediate stiffness. This behavior highlights the mechanical coupling between wood and polymer and the efficiency of stress transfer at the interface for both chamfer configurations. The stiffness of the wood is approximately one order of magnitude higher than that of the polymer. As expected for hybrid structures, the joint exhibits an intermediate effective stiffness governed by the elastic properties of the constituent materials, their geometric distribution, and the interfacial mechanical coupling. The curves corresponding to the two faces, for each component as well as for the joint as a whole, show a high degree of agreement. Minor differences observed in the wood curves can be attributed to its intrinsic heterogeneity, associated with anisotropy and the non-uniform distribution of vessels. The strong overlap of the curves indicates nearly symmetric mechanical behavior across the joint thickness, with no evidence of significant strain gradients, suggesting negligible secondary bending effects during testing.

Figure 10 presents the normalized equivalent strains obtained by DIC on each face of the components of the PA6–Eucalyptus joints with single- and double-chamfer configurations, calculated from the last image acquired immediately prior to joint failure. The equivalent strains

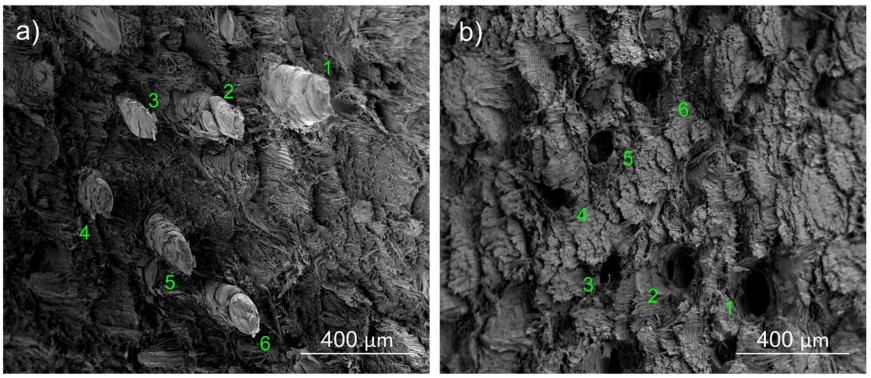



**Figure 8.** SEM images of the delaminated fracture surfaces of the PA6–Eucalyptus joints after mechanical testing. The polymer side is shown on the left (a) and the wood side on the right (b).

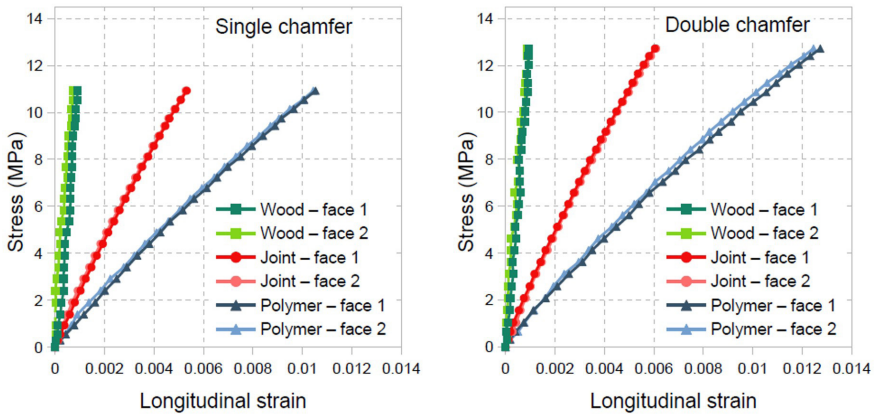



**Figure 9.** Longitudinal stress–strain curves obtained from mechanical tests coupled with DIC for the PA6–Eucalyptus scarf joints in the single- and double-chamfer configurations.

shown in Figure 10 were parameterized by dividing the value of each element by the corresponding mean value of each joint component obtained from the virtual strain gauges (Figure 2). This procedure was adopted due to the significant difference in stiffness between the materials (Figure 9). This parameterized strain therefore constitutes a type of strain concentration factor, allowing a direct comparison of the relative strain distribution within each joint component and enabling the identification of regions of strain concentration or redistribution along the joint interface.

For the single-chamfer configuration, equivalent strain fields exhibit a more gradual and relatively homogeneous distribution along the interface, in both the polymer component and the wood substrate. This behavior indicates a more progressive load transfer between the materials along the chamfer region. In contrast, the double-chamfer configuration shows a more pronounced concentration of equivalent strains in the region of the upper chamfer vertex. The strain maps reveal steeper gradients in this region, suggesting that load transfer occurs in a more localized manner. Additionally, the strain fields in the wood exhibit a more spatially confined distribution, reflecting its higher stiffness, whereas in the PA6 component the strains extend over a broader region above the interface. This behavior highlights the role of the polymer in accommodating the overall deformation of the joint and in redistributing the stresses transferred to the wood substrate.

## 4. Conclusions

Joints composed of polyamide 6 and *Eucalyptus grandis* wood were successfully produced by direct-adhesion injection overmolding using single- and double-chamfer scarf geometries. SEM and X-ray microtomography analyses revealed a well-defined polymer–wood interface, with PA6 penetrating open wood vessels and forming protrusions (~50 µm) that promote mechanical interlocking. Mechanical tests showed low dispersion and shear strengths of 8.1 ± 0.6 MPa and 7.3 ± 1.0 MPa for the single- and double-chamfer configurations, respectively, comparable to values reported for other polymer–wood joints. Fractographic observations indicated a mixed adhesive–cohesive failure mode, involving polymer extraction from wood vessels and localized cohesive failure within the wood and the polymer. DIC revealed effective mechanical coupling between the components, with the joint exhibiting an intermediate effective stiffness between those of the constituent materials. Strain-field analysis indicated that the single-chamfer configuration

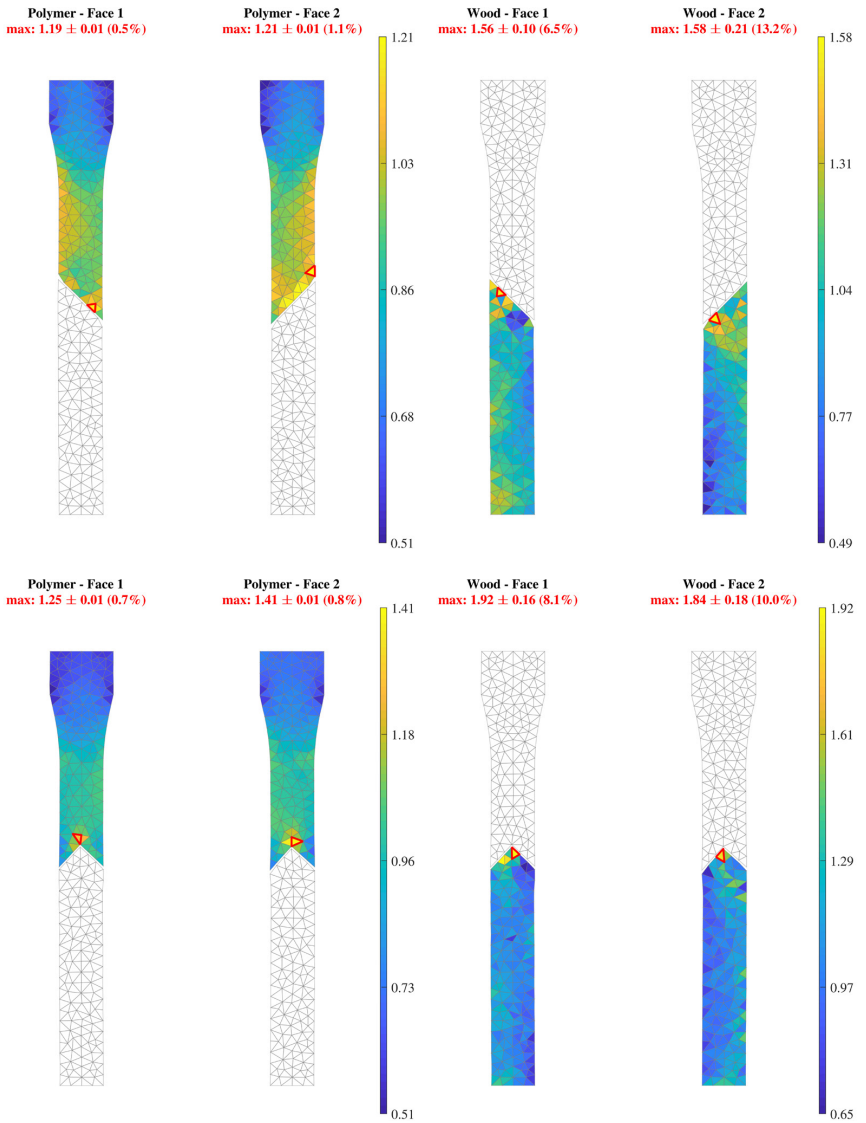



**Figure 10.** Normalized equivalent strains obtained by DIC on each face of the components of the PA6–Eucalyptus joints with single- and double-chamfer configurations.

promotes a more uniform strain distribution along the interface, whereas the double-chamfer geometry leads to more localized strain concentrations.

## 5. Author's Contribution

- **Conceptualization** – Leonardo Bresciani Canto.
- **Data curation** – Giovana Zanetini Zanchetta; Gean Henrique Marcatto de Oliveira; Matheus Furlan; Rodrigo Bresciani Canto; Leonardo Bresciani Canto.
- **Formal analysis** – Giovana Zanetini Zanchetta; Gean Henrique Marcatto de Oliveira; Matheus Furlan; Vinicius Fiocco Sciuti; Rodrigo Bresciani Canto; Leonardo Bresciani Canto.
- **Funding acquisition** – Leonardo Bresciani Canto.
- **Investigation** – Giovana Zanetini Zanchetta; Gean Henrique Marcatto de Oliveira; Matheus Furlan; Rodrigo Bresciani Canto; Leonardo Bresciani Canto.
- **Methodology** – Rodrigo Bresciani Canto; Leonardo Bresciani Canto.
- **Project administration** – Leonardo Bresciani Canto.
- **Resources** – Giovana Zanetini Zanchetta; Gean Henrique Marcatto de Oliveira; Rodrigo Bresciani Canto; Leonardo Bresciani Canto.
- **Software** – Matheus Furlan; Vinicius Fiocco Sciuti.
- **Supervision** – Gean Henrique Marcatto de Oliveira; Leonardo Bresciani Canto.
- **Validation** – Giovana Zanetini Zanchetta; Gean Henrique Marcatto de Oliveira; Rodrigo Bresciani Canto; Leonardo Bresciani Canto.

- **Visualization** – Giovana Zanetini Zanchetta; Gean Henrique Marcatto de Oliveira; Rodrigo Bresciani Canto; Leonardo Bresciani Canto.
- **Writing – original draft** – Giovana Zanetini Zanchetta; Gean Henrique Marcatto de Oliveira; Leonardo Bresciani Canto.
- **Writing – review & editing** – Giovana Zanetini Zanchetta; Gean Henrique Marcatto de Oliveira; Matheus Furlan; Vinicius Fiocco Sciuti; Rodrigo Bresciani Canto; Sergio de Traglia Amancio Filho; Leonardo Bresciani Canto.

## 6. Acknowledgements

This study was financed in part by the Coordenação de Aperfeiçoamento de Pessoal de Nível Superior - Brasil (CAPES) – Finance Code 001. This study was supported by CNPq – National Council for Scientific and Technological Development, Brazil (307914/2023-2, 443861/2024-2, 309266/2022-0). This research was supported by the Brazilian National Council for Scientific and Technological Development (CNPq) through the INCT Circularity in Polymer Materials (406925/2022-4). This study was financed, in part, by the São Paulo Research Foundation (FAPESP), Brasil, process number # 2024/08861-0.

## 7. References

1. Amancio-Filho, S. T., & Blaga, L. A. (Eds.). (2018). *Joining of polymer-metal hybrid structures: principles and applications*. Hoboken: John Wiley & Sons. https://doi.org/10.1002/9781119429807.
2. Ding, Y., Pang, Z., Lan, K., Yao, Y., Panzarasa, G., Xu, L., Lo Ricco, M., Rammer, D. R., Zhu, J. Y., Hu, M., Pan, X., Li, T., Burgert, I., & Hu, L. (2023). Emerging engineered wood for building applications. *Chemical Reviews*, *123*(5), 1843-1888. https://doi.org/10.1021/acs.chemrev.2c00450. PMid:36260771.
3. Schubert, M., Panzarasa, G., & Burgert, I. (2023). Sustainability in wood products: a new perspective for handling natural diversity. *Chemical Reviews*, *123*(5), 1889-1924. https://doi.org/10.1021/acs.chemrev.2c00360. PMid:36535040.
4. Asada, R., Cardellini, G., Mair-Bauernfeind, C., Wenger, J., Haas, V., Holzer, D., & Stern, T. (2020). Effective bioeconomy? a MRIO-based socioeconomic and environmental impact assessment of generic sectoral innovations. *Technological Forecasting and Social Change*, *153*, 119946. https://doi.org/10.1016/j.techfore.2020.119946.
5. Kohl, D., Link, P., & Böhm, S. (2016). Wood as a technical material for structural vehicle components. *Procedia CIRP*, *40*, 557-561. https://doi.org/10.1016/j.procir.2016.01.133.
6. Vasconcelos, R. L., Oliveira, G. H. M., Amancio-Filho, S. T., & Canto, L. B. (2023). Injection overmolding of polymer-metal hybrid structures: a review. *Polymer Engineering and Science*, *63*(3), 691-722. https://doi.org/10.1002/pen.26244.
7. Oliveira, G. H. M., Amancio-Filho, S. T., & Canto, L. B. (2024). Processing understanding, mechanical durability and hygrothermal stability of PC/AA6061 hybrid joints produced via injection overmolding. *International Journal of Adhesion and Adhesives*, *130*, 103617. https://doi.org/10.1016/j.ijadhadh.2023.103617.
8. Adauto, R., Oliveira, G. H. M., Morozo, M. A., Fiori, M. A., & Canto, L. B. (2025). Direct-joining of a polylactide acid-hydroxyapatite biocomposite with a titanium alloy. *Polímeros: Ciência e Tecnologia*, *35*(1), e20250009. https://doi.org/10.1590/0104-1428.20240095.
9. Stadlmann, A., Mautner, A., Pramreiter, M., Bismarck, A., & Müller, U. (2021). Interfacial adhesion and mechanical properties of wood-polymer hybrid composites prepared by injection molding. *Polymers*, *13*(17), 2849. https://doi.org/10.3390/polym13172849. PMid:34502888.
10. Palermo, G. P. M., Latorraca, J. V. F., Carvalho, A. M., Calonego, F. W., & Severo, E. T. D. (2015). Anatomical properties of *Eucalyptus grandis* wood and transition age between juvenile and mature wood. *Holz als Roh- und Werkstoff*, *73*(6), 775-780. https://doi.org/10.1007/s00107-015-0947-4.
11. Leclerc, H., Neggers, J., Mathieu, F., Roux, S., & Hild, F. (2015). *Correli 3.0.* Paris: Agence pour la Protection des Programmes.
12. Lubliner, J. (2008). *Plasticity theory.* Mineola: Dover Publications.
13. Mendelson, A. (1968). *Plasticity: theory and application.* New York: Macmillan.
14. Gardner, D. J., Blumentritt, M., Wang, L., & Yildirim, N. (2014). Adhesion theories in wood adhesive bonding: a critical review. *Reviews of Adhesion and Adhesives*, *2*(2), 127-172. https://doi.org/10.7569/RAA.2014.097304.
15. Oliveira, G. H. M., Awan, A., Auer, P., Egger, P.-M., Canto, L. B., Domitner, J., & Amancio-Filho, S. T. (2026). Direct-joining of short carbon fiber-reinforced polyamide 6 composite with wood by additive manufacturing. *Progress in Additive Manufacturing*, *11*(5), 4917-4931. https://doi.org/10.1007/s40964-026-01632-9.
16. Awan, A., Oliveira, G. H. M., Carvalho, W. S., Auer, P., Domitner, J., & Amancio-Filho, S. T. (2024). Ultrasonic joining of carbon-reinforced polyamide with oak wood for manufacturing sustainable hybrid structures. *Manufacturing Letters*, *42*, 26-29. https://doi.org/10.1016/j.mfglet.2024.09.068.
17. Oliveira, G. H. M., Sciuti, V. F., Canto, R. B., Arneitz, S., Minkowitz, L., Amancio-Filho, S. T., & Canto, L. B. (2025). Additive manufacturing of surface structured metal parts for high strength lightweight injection overmolded polymer-metal hybrid joints. *International Journal of Adhesion and Adhesives*, *141*, 104045. https://doi.org/10.1016/j.ijadhadh.2025.104045.

*Received: Apr. 03, 2026*
*Revised: May 20, 2026*
*Accepted: June 10, 2026*

**Editor-in-Chief:** *Sebastião V. Canevarolo*